OBSERVATIONS OF COMPLEX TERRAIN FLOWS USING ACOUSTIC SOUNDERS: ECHO INTERPRETATION

W. D. NEFF

NOAA/ERL/Wave Propagation Laboratory, Boulder, CO 80303, U.S.A.

(Received in final form 23 June, 1987)

Abstract. We examine methods for the interpretation of sodar facsimile records obtained in the study of complex terrain flows. Acoustic scattering theory is presented first and then interpreted using a simpolified second-order turbulence closure scheme. The use of this theory suggests the strong sensitivity of acoustic scatter to changes in the wind shear. With this introduction, detailed sodar facsimile records, temperature and wind profiles, and model calculations follow. Characteristic scattering patterns are described for simple drainage jets, complex basin flows, convection with a capping inversion, stratus, and dynamical instabilities. Examples are also shown of bistatic facsimile records detailing the strong temporal and spatial variability of small-scale turbulence.

1. Introduction

The first part of this series (Neff and King, 1987), outlined a sequence of experiments carried out by the U.S. Department of Energy's Atmospheric Studies in Complex Terrain (ASCOT) program in which Doppler sodars were used. That paper described the topography and meteorology of the sites used in the experiments, and the behaviour of the Doppler-derived wind fields in a variety of circumstances. The Doppler sodars used in the study of complex terrain flows in fact mimicked conventional instrumentation, differing primarily in spatial and temporal averaging characteristics. Acoustic remote sensing, however, depends integrally on the presence and distribution of turbulent temperature and velocity fluctuations at scales less than 1 m. The distribution of this microstructure affects and sometimes limits the ability of Doppler sodars to profile the wind; at the same time, the echo patterns produced by sodars should reflect the processes responsible for the production of turbulence. Because of this, there is some hope that sodar facsimile recordings can be used to identify the variety of physical processes important to the complex terrain flows studied in the ASCOT and similar experiments.

In this paper we focus on the interpretation of acoustic echoes in complex terrain flows. We begin with a discussion of the scattering theory and simplifications possible for stably-stratified flow: this permits an interpretation of the scattering in terms of vertical potential temperature gradients and wind shear. The scattering theory is presented for both monostatic sounding (colocated transmitter and receiver) and bistatic sounding (separated transmitter and receiver) configurations; in the monostatic mode, sound scatters only from small-scale thermal inhomogeneities whereas in the bistatic mode it also scatters directly from small-scale velocity fluctuations. We then describe the characteristic monostatic echo patterns that arise in a variety of circum-

Boundary-Layer Meteorology **42** (1988) 207–228.

stances: (1) simple slope drainage, (2) channeled flows, (3) basin flows, (4) convection with a capping inversion, (5) stratus, and (6) dynamical instability. In the description of stably-stratified shearing flow, we shall introduce the use of a second-order turbulence parameterization as a technique with which to interpret sodar echo patterns: because such models calculate turbulence quantities in terms of mean gradients, we make use of wind and temperature profiles to calculate scattering profiles and then compare these results with actual sodar observations.

2. Acoustic Scattering

Our analysis of ASCOT sodar data, obtained under mostly stably-stratified conditions, will use the interpretative approach suggested by Neff and Coulter (1986). Their line of reasoning begins with the classical expression for the acoustic differential scattering cross-section per unit volume written in terms of isotropic, three-dimensional spectral densities of temperature and turbulent kinetic energy. Through the use of inertial-subrange expressions for the spectra, the scattering cross-section assumes the form

$$\sigma(\theta_s) = \tfrac{1}{8}k^4 K^{-11/3} \cos^2(\theta_s)\left[\frac{0.106 N_\theta \varepsilon^{-1/3}}{T_0^2} + \frac{\cos^2(\theta_s/2)}{\pi C_0^2}\ 1.5\varepsilon^{2/3}\right], \tag{1}$$

where k is the acoustic wave number; K the Bragg wave number, $K = 2k \sin(\theta_s/2)$; θ_s, the scattering angle from the direction of propagation; N_θ, the rate of destruction of one-half of the temperature variance; ε, the energy dissipation rate; T_0, the local absolute temperature; and C_0, the local speed of sound. They also describe the alternative expression

$$\sigma(\theta_s) = \tfrac{1}{8}k^4 K^{-11/3} \cos^2(\theta_s)\left[\frac{0.033 C_T^2}{T_0^2} + \frac{\cos^2(\theta_s/2)}{\pi C_0^2}\ 0.76 C_V^2\right] \tag{2}$$

written in terms of the temperature structure function

$$C_T^2 = \langle [T(\mathbf{x} + \mathbf{r}) - T(\mathbf{x})]^2 \rangle / r^{2/3} \tag{3}$$

and the velocity structure function

$$C_V^2 = \langle [U(\mathbf{x} + \mathbf{r}) - U(\mathbf{x})]^2 \rangle / r^{2/3}, \tag{4}$$

where measurements are made at two locations $\mathbf{x}$ and $\mathbf{x} + \mathbf{r}$, and where $\langle\ \rangle$ indicates an ensemble average, normally approximated by a time-average in practical applications.

The most familiar sodar data come from monostatic systems, a configuration in which only the temperature spectrum contributes to the scattering; in the case of stably-stratified flow, simplification of the conservation equation for the temperature variance leads to an equation useful for the interpretation of such records, namely

$$\sigma(180°) = (0.105/8)\,(k^{1/3}/T_0^2) K_H^{2/3} [\mathrm{Rf}/(1 - \mathrm{Rf})]^{1/3} \left(\frac{\partial \theta}{\partial z}\right)^{5/3} \tag{5}$$

where $\partial\theta/\partial z$ is the vertical gradient of potential temperature and Rf is the flux Richardson number defined by

$$\mathrm{Rf} = \mathrm{Ri}(K_H/K_M)\,, \tag{6}$$

where K_H and K_M are the eddy diffusion coefficients for heat and momentum, respectively. The gradient Richardson number is defined by

$$\mathrm{Ri} = \frac{g}{T_0}\,\frac{\partial\theta/\partial z}{\left[\left(\frac{\partial U}{\partial z}\right)^2 + \left(\frac{\partial V}{\partial z}\right)^2\right]} \tag{7}$$

written in terms of the vector wind shear.

Equation (5) shows that the acoustic backscatter depends most strongly on the vertical temperature gradient and on an eddy diffusion coefficient that quantifies the local turbulent mixing. The eddy diffusion coefficient, in turn, depends strongly on Ri and, hence, on the vertical shear of the horizontal wind because it enters quadratically in (7).

3. Modeling of Acoustic Scatter

Whereas the above descriptions provide qualitative insight into acoustic scattering, they lack practical quantitative substance. However, because second-order turbulence closures provide simple diagnostic relationships between turbulence quantities and local mean gradients of wind and potential temperature, they provide an appealing approach to this problem and a tool with which to study turublent scattering processes (Burk, 1980; Neff, 1980). Following Neff (1980), we have used the parameterizations proposed by Brost and Wyngaard (1978, 1979) and described in a succinct form by Fitzjarrald (1979), to analyze scattering cross-sections and to calculate acoustic backscatter profiles from observed wind and temperature profiles.

We have described the model in the appendix together with a number of tests that we applied to determine our level of confidence in its application. Our use of this model requires a few caveats. First, because of the simple model closures, all turbulence values are calculated directly as a function of Ri and are set to zero for Ri above a critical value. This ignores the possibility that turbulence, once generated, can persist up to an Ri = 1.0; models that include higher order closures deal with this problem more directly. (However, such models are necessarily prognostic because the scattering profile will depend on the history of the flow; they thus lack the utility of simple diagnostic models.) Second, because of the dependence of turbulence on Ri and the neglect of triple correlations, the model may not deal very effectively with the large Ri region at the nose of jets; only when there is strong azimuthal shear across the jet will Ri remain below its critical value. Our use of the model to calculate C_T^2 profiles from observed wind and temperature data is thus only a first semi-quantitative step in the interpretation of sodar echo patterns.

Some indication of the behavior of the scattering predicted by (2) can be obtained from the model. In particular, we calculated a number of scattering properties using the model, as shown in Figures 1a, b, c, and d. In Figure 1a, we show C_T^2 as a function of Ri for values of shear from 0.01 to 0.10 s^{-1}; in Figure 1b we show similar curves for C_V^2. In each case, following each curve reveals the effect of increasing static stability on the acoustic scatter for a given value of shear; the displacement in the vertical from curve to curve for a constant value of Ri shows the effect of increasing shear for a given static stability. For a given value of shear, C_T^2 increases with increasing temperature gradient up to an Ri of about 0.12 and, thereafter, decreases with increasing stability as the turbulent mixing becomes weaker. The behavior of C_V^2 in Figure 1b shows its sensitivity to increasing Ri (for constant shear). Of particular note in these results is the strong sensitivity of the scattering to changes in static stability at large and small Ri and the sensitivity to changes in the shear at all stabilities. For example, a change in shear from 1 to 2 m s^{-1} over 100 m produces more than an order of magnitude increase in C_T^2, suggesting that echo patterns observed with sodars ought to reflect a strong sensitivity to meteorological processes affecting wind shear.

The model also allows comparison of the relative contributions to the scattering from C_T^2 and C_V^2. In Figure 1c, we evaluate the relative contributions of C_T^2 and C_V^2 to forwardscatter at an angle of 120 deg, a typical bistatic Doppler-scattering angle, taking the ratio of the two terms in brackets in (2) for various stabilities and shear. These results indicate that scattering from velocity fluctuations dominate for all but the largest values of Ri and weak shear. In Figure 1d, we examine the ratio of backscatter to forward-scatter cross-sections as a function of Ri and shear. In this example, forwardscatter exceeds backscatter for all but the largest values of Ri. The utility of bistatic Doppler sodar systems would thus appear to be limited primarily by that portion of the system design dealing with the illumination of the scattering volumes (the transmitted beam is fanned to illuminate a larger section of the vertical receiving beam). For example, if the bistatic illumination is 0.10 of the monostatic, then for those portions of the curves above the 0.10 line, monostatic systems will be more effective: in this model calculation, these curves span a significant range of shear and static stability. With large Ri and weak shear, the results in Figure 1d suggest that monostatic systems would be more effective.

4. Temperature and Wind Structure in Drainage Flows

The model results described above suggest that the interpretation of sodar echoes requires coincident and detailed wind and temperature profiles. Neff and King (1987), using tethered balloon data, described typical temperature profiles that occur in nocturnal inversions in complex terrain. On steep slopes, radiative cooling, and the subsequent redistribution of heat by long-wave radiation and turbulent mixing near the surface, causes a shallow katabatic inversion layer, often less than 50 m depth. Because of the steep slopes, they found that Archimedean forces dominate in these regions. In contrast, in basin areas, the inversion builds to a depth of several hundred meters as cool air accumulates in low-lying regions. Because of the lesser slopes, Archimedean

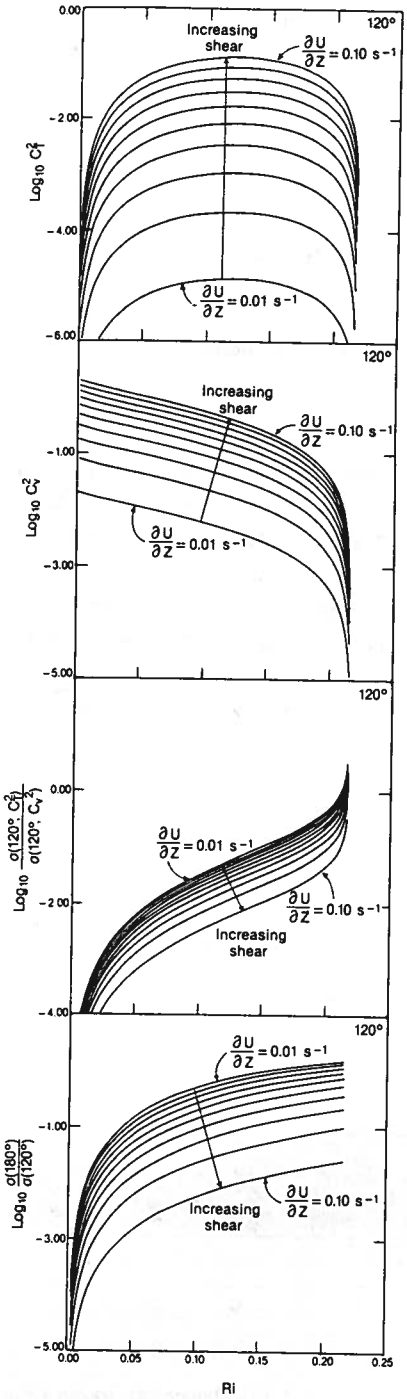

Fig. 1a

Fig. 1b.

Fig. 1c.

Fig. 1d.

Fig. 1. (a) Behavior of C_T^2 as a function of shear and Ri, using model parameterization described in the Appendix. (b) Behavior of C_V^2. (c) Relative contributions of C_T^2 and C_V^2 to forward scatter at an angle of 120°, as functions of shear and Ri. (d) Ratio of backscatter to forwardscatter (120°) cross-sections as functions of shear and Ri.

forces were comparable to those of synoptic and mesoscale origin. Neff and King (1987) also described characteristic wind profiles observed in both simple and complex drainage flows using both Doppler sodars and tethered balloon soundings: over simple slopes and in draining valleys, wind profiles were simple, usually with a single wind maximum; in basins subject to topographic constriction and/or blocking by an ambient pressure gradient (such as the marine inversion in the Geysers), winds were light and variable with height and in time. In these data, the Doppler sodar wind profiles had a typical vertical resolution of 25 m, the tethered balloon of about 4 to 10 m.

5. Monostatic Echo Structure

5.1. Simple slopes

Stably-stratified flows dominated by frictional interaction with a rough boundary provide examples of the most simply-structured echo layers observed with sodars (Neff, 1980; Neff and Coulter, 1986). In such cases, strong shear near the surface overcomes the effect of a statically stable lapse rate, producing turbulence; the resulting turbulent mixing and long-wave radiative flux divergence then communicates the effect of radiative cooling of the surface to the interior of the boundary layer causing a stable lapse rate. This then provides the necessary ingredients to produce acoustic scattering as predicted by (5): a positive $\partial\theta/\partial z$ and non-zero eddy diffusion coefficient, K_H. In a katabatic flow over a simple slope, complications ensue. In particular, with a low-level wind maximum,

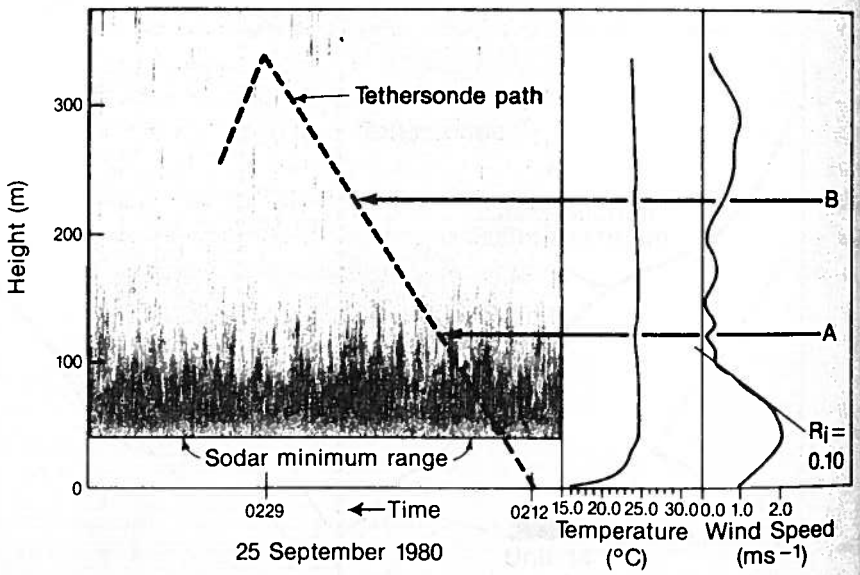

Fig. 2. Sodar facsimile record corresponding to shallow drainage flow on an elevated slope displayed with simultaneous wind and temperature profiles. The top of the drainage flow is denoted by A. A second, weak, elevated inversion and scattering layer is identified with the label B. The strongest echoes occur in the region above the jet where Ri ~ 0.10.

mesoscale origin. Neff and King
observed in both simple and c
nd tethered balloon soundings: over
files were simple, usually with a sing
hic constriction and/or blocking by an a
version in the Geysers), winds were li
e data, the Doppler sodar wind profile
thered balloon of about 4 to 10 m.

c Echo Structure

ctional interaction with a rough bo
tured echo layers observed with sodar
ses, strong shear near the surface over
producing turbulence; the resulting tur
nce then communicates the effect of ra
e boundary layer causing a stable laps
ts to produce acoustic scattering as pre
diffusion coefficient, K_H. In a katabat
n particular, with a low-level wind max

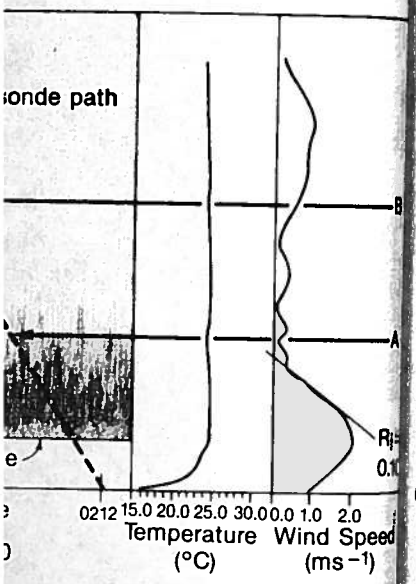

ow drainage flow on an elevated slope displa
of the drainage flow is denoted by A. A secon
h the label B. The strongest echoes occur in th
here Ri ~ 0.10.

ere are regions of strong shear both near the surface and above the wind maximum
elf. When such shear becomes large enough, turbulence results, producing momentum
nsfers that try to balance the katabatic force due to the increasing temperature deficit
er the slope (Manins and Sawford, 1979; Horst and Doran, 1986). This same
rbulence should also produce acoustic scattering as suggested by the results shown
Figure 2, where we have used tethersonde and sodar data from the Unit 19 site
erated by the Pacific Northwest Laboratory (PNL). In this case, the major tempera-
re deficit and wind maximum are below the minimum range of the sodar. However,
e band of strongest echoes above the minimum range corresponds to the strongly-
earing region above the jet maximum where Ri = 0.10. In the figure, we have indicated
o weak elevated inversions, each corresponding to a temperature change of less than
5 °C. The first, labeled A, corresponds roughly to the top of the mixing region above
e jet; the second, labeled B, corresponds to a weak echo region on the sodar record
t below a region of increasing wind shear and slightly stronger stability.

2. Draining and Channeling Valleys

ce individual slope flows accumulate, they are generally channeled by the larger-scale
ley system. In the upper portions of Big Sulphur and Brush Creeks, the resulting wind
d is fairly steady with a well-defined wind maximum. Figure 3 shows the V-shaped

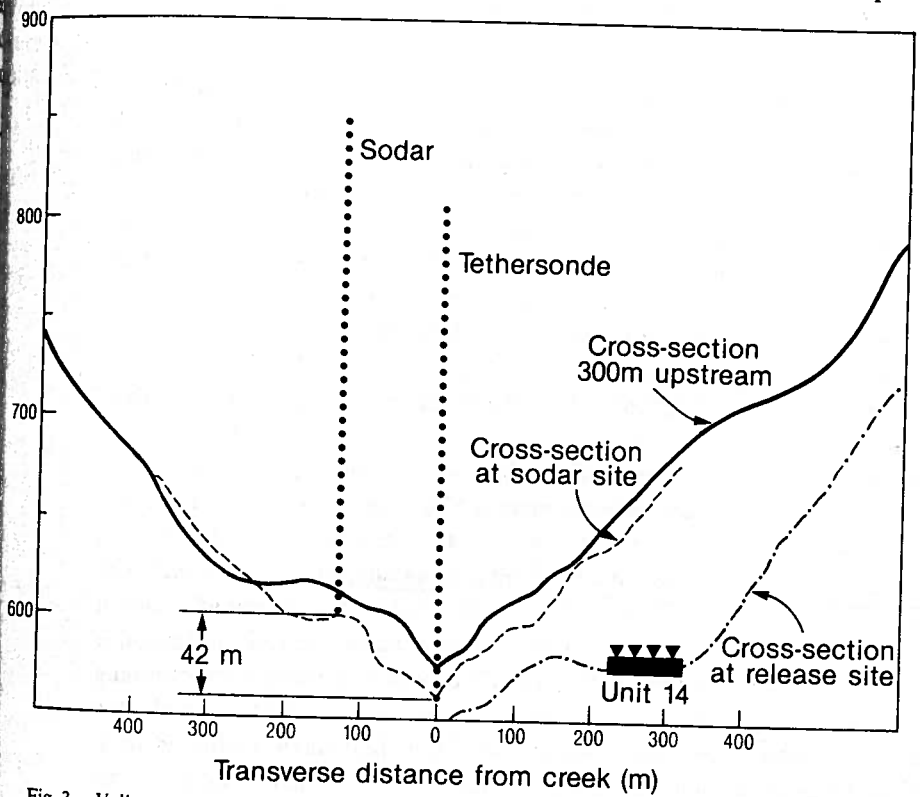

Fig. 3. Valley cross-section and profile locations for Unit 14 site in Big Sulphur Creek.

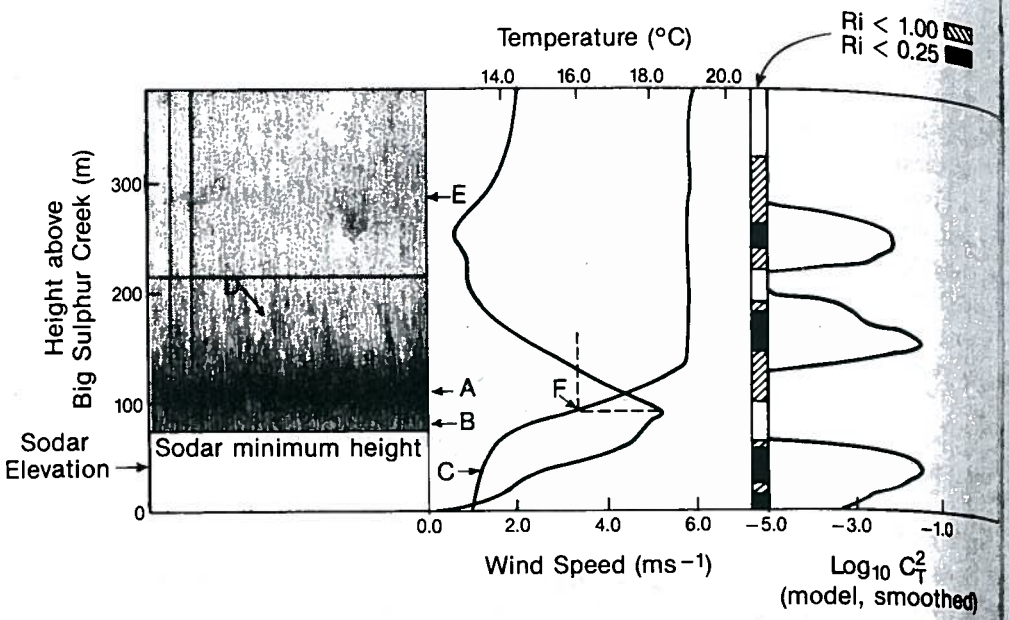

Fig. 4. Sodar facsimile recording during well-developed drainage flow at Unit 14 together with wind and temperature profiles and model-calculated scattering profiles. Labels are keyed to the text.

valley cross-section at the Unit 14 site in Big Sulphur Creek and the relative locations of sodar and tethersonde profiles. The downstream location of the Unit 14 power plant is also shown. Figure 4 displays a typical facsimile record, associated temperature and wind profiles obtained within the drainage flow, an indication of regions in which $Ri < 1.0$ and $Ri < 0.25$, and the profile of C_T^2 calculated with the model described in Section 3. The temperature and wind data were obtained with a tethered balloon system. The vertical sampling interval was about 4 m and we smoothed the profiles with a triangular filter. The calculated C_T^2 profile, non-zero only where $Ri < 0.22$, was smoothed with a 30-m block filter that corresponded to the acoustic pulse length used in the observations. Several features (keyed to the figure) are evident in comparing the data and calculations:

(a) The dark echo band corresponds to the region of reduced Ri above the jet, as in 5.1. The region in which $Ri < 0.25$ is more elevated than the observed echo pattern; this may arise from two causes. First, the fact that turbulence once generated can persist to values of $Ri = 1.0$ would imply a thicker scattering region than that predicted by the model. The region of $Ri < 1.0$ in Figure 4 corresponds more closely to the actual sodar echo region. Second, because of the irregularity of the underlying terrain, there is no guarantee of horizontal homogeneity. Also of interest is the location of the maximum echo layer relative to the temperature inversion, as calculated with the model: namely, at its boundary. Examination of Figure 1a shows that for constant shear (as above the jet maximum in Figure 4), C_T^2 rapidly decreases with increasing stability. This suggests that sodar echo layers may at times delineate the boundaries of temperature inversions rather than the inversion itself.

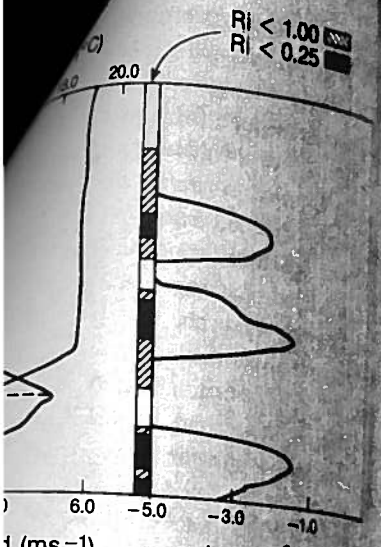

ıge flow at Unit 14 together with wind and ofiles. Labels are keyed to the text.

ır Creek and the relative locations ɔcation of the Unit 14 power plant. ɛcord, associated temperature and n indication of regions in which ated with the model described in ıed with a tethered balloon system. we smoothed the profiles with a ero only where $Ri < 0.22$, was to the acoustic pulse length used ure) are evident in comparing the

of reduced Ri above the jet, as in ın the observed echo pattern; this lence once generated can persist region than that predicted by the s more closely to the actual sodar ıe underlying terrain, there is no t is the location of the maximum lculated with the model: namely, for constant shear (as above the ncreasing stability. This suggests ıdaries of temperature inversions

(b) The weaker echo region below the band described in (a) corresponds to a maximum in Ri at the nose of the jet where the wind shear is least.

(c) The temperature profile near the surface is nearly isothermal, suggesting that surface radiative cooling is not sufficient to maintain a stable lapse rate against the strong shear-induced mixing below the jet. Such isothermal layers below elevated drainage jets have also been observed in Antarctica and modeled numerically in cases of weak surface cooling (Neff, 1980), a situation corresponding to a nearly balanced surface energy budget.

(d) Intermittent turbulence occurs above the jet at periods on the order of tens of minutes.

(e) A weak echo layer occurs at a weak elevated inversion (~250 m) and marks the boundary between the down-valley flow and northerly winds above.

(f) The maximum of the jet occurs at a point corresponding to about one half of the maximum temperature deficit.

5.3. Basins and Pooling Regions

In sodar observations of simple slope and channeled draining flows described above, echo patterns were generally well defined and similar in a variety of locations. However, in basins and pooling regions, echo patterns are typically more complex, their primary characteristic being the stratification and irregularity of the echo strata as shown in Figure 5. In this case, the tethered-balloon sounding obtained data at 10-m intervals;

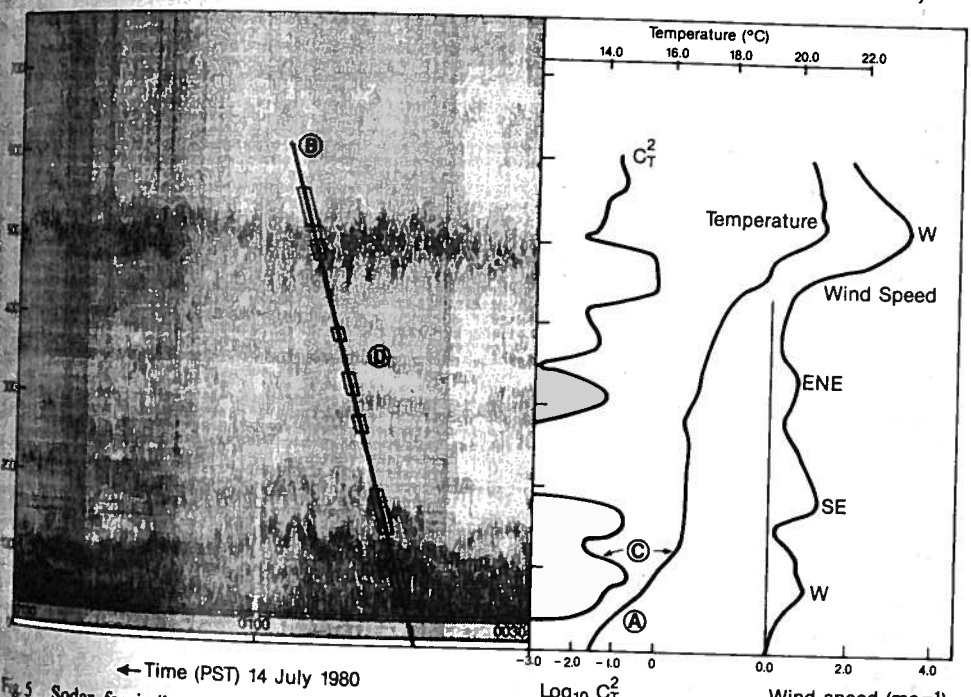

Fig. 5 Sodar facsimile recording showing simultaneous wind and temperature profiles and model-calculated scattering profiles. The figure is keyed to the text.

because of this larger interval, we used no filtering on the data used to calculate C_T^2, but did filter the profiles of C_T^2, wind speed and temperature for presentation in the figure. The wind profile in this case is similar to those given in Neff and King (1987) during a period of strong marine inversion influence, viz, low speeds and highly variable directions. Some of the findings of this comparison are:

(a) The temperature profile consists of three parts, a strong surface inversion to about 150 m, an isothermal layer between 150 and 250 m, and increasing stability and a stronger capping inversion at 500 m.

(b) We overlayed the approximate path of the tethersonde on the sodar facsimile record and indicated regions in which Ri is reduced below 1.0. These correspond roughly, as do the calculated values of C_T^2 (smoothed as before), to the observed echo layers.

(c) The strongest echo layers occur near the boundaries of the regions of greatest temperature gradient as seen previously in Figure 4.

(d) Multiple echo layers correspond to thin regions in which Ri is reduced.

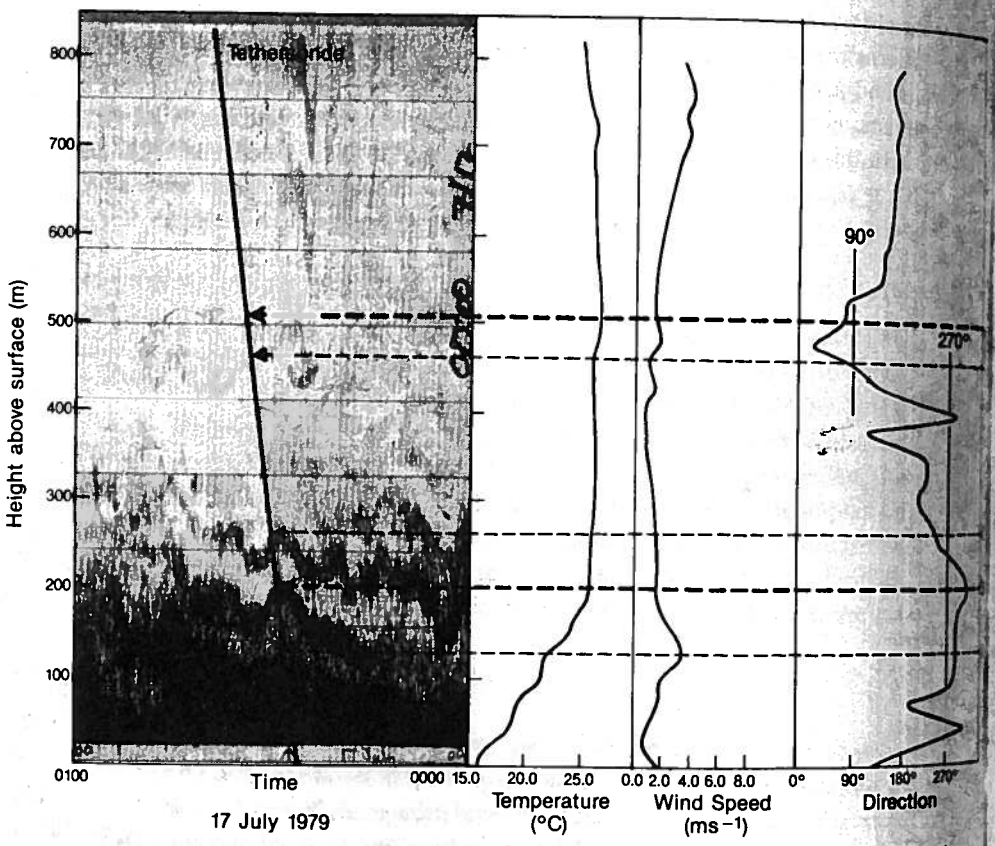

Fig. 6. Sodar facsimile recording together with simultaneous temperature, wind speed, and wind direction profiles showing the dependence of scattering layers on azimuthal shear under light wind conditions. The figure is keyed to the text.

A second exampl
and small changes
produce a variety o
(a) Local wind n
(b) The height of
surface-based echo
(c) Regions of str
the wind speed vari
hence turbulence, d
(d) The temperatu
meters in contrast t
the pooled flow and
in response to char
Examination of th
in wind speed and l
the lapse is nearly is
direction varies by
we argued that echo
small. If one takes a
of 90 deg over 25 m
Ri = 0.10, a value
Figure 1, using thes
0.01 °C² m⁻²/³ de

5.4. Convection

With the onset of
activity form. Such
geneities from the l
magnitude of the
magnitudes decrea
mixing produced b
the buoyant parcel
in Kaimal *et al.* (19
terrain with slopes
the echo patterns.

5.5. Stratus

In Neff and King
significant influenc
even more direct, a
low clouds fill the v
itself. In Figure 8,
the layer of strong
observation from t

A second example is provided in Figure 6 where winds are light throughout the profile and small changes in wind speed combine with larger changes in wind azimuth to produce a variety of thin scattering layers:

(a) Local wind maxima produce minima in the scattering as before.

(b) The height of the surface-based inversion corresponds to the region of strongest surface-based echoes.

(c) Regions of stronger azimuthal shear produce isolated scattering layers even though the wind speed varies little. This follows from the fact that the Richardson number, and hence turbulence, depend on the vector shear as in Equation (7).

(d) The temperature profile often shows a weak elevated inversion at several hundred meters in contrast to the results in Figure 5. Because this is often the boundary between the pooled flow and the ambient wind, a distinct, although weak, echo layer often forms in response to changes in wind speed and direction across this airmass boundary.

Examination of these figures shows an association of echo strata with small variations in wind speed and larger variations in wind direction in thin layers: often in these cases the lapse is nearly isothermal, the wind speed varies from 0.0 to 2.0 m s^{-1}, and the wind direction varies by as much as 90 deg over a height of 25 m. In our discussion of (5), we argued that echo regions should be closely connected with regions in which Ri was small. If one takes a wind speed of 1.0 m s^{-1}, an isothermal lapse, and a direction shift of 90 deg over 25 m (not unusual in such light wind conditions), Equation (7) predicts Ri = 0.10, a value sufficiently small to expect instability and turbulence. Refering to Figure 1, using these values of Ri and shear, suggests a relatively large value of C_T^2 of 0.01 $°C^2\,m^{-2/3}$ despite the relatively small temperature gradient.

5.4. Convection with a Capping Inversion

With the onset of solar heating in the morning, echoes characteristic of convective activity form. Such echoes, as shown in Figure 7, result when temperature inhomogeneities from the heated surface are carried upward by buoyant plumes. Because the magnitude of the inhomogeneities decreases as mixing continues, convective echo magnitudes decrease with height on average. In the presence of a capping inversion, the mixing produced both by the shear, if any, in the ambient wind, and by the impact of the buoyant parcels results in scattering layers as evident in Figure 7 and as described in Kaimal *et al.* (1982). In the facsimile recording in this figure, obtained over complex terrain with slopes between 0.1 and 0.2, there is little evidence of terrain influence on the echo patterns.

5.5. Stratus

In Neff and King (1987), it was proposed that the marine inversion could have a significant influence on drainage flows in the Geysers area. At times, the connection is even more direct, as the depth of the marine layer increases to the point that fog and low clouds fill the valleys to the west and northwest and flow over the Mayacmas ridge itself. In Figure 8, we show echoes from the top of such a stratus layer. The fact that the layer of strong echoes lies near the top of the stratus layer was verified by direct observation from the ridge above the valley.

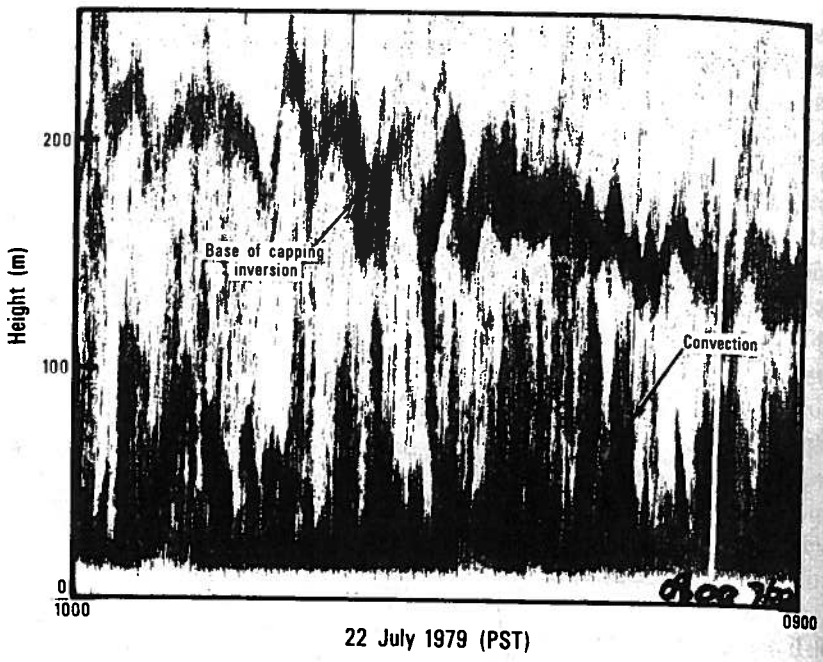

Fig. 7. Example of sodar echo patterns in the case of convection from a heated slope together with a capping inversion.

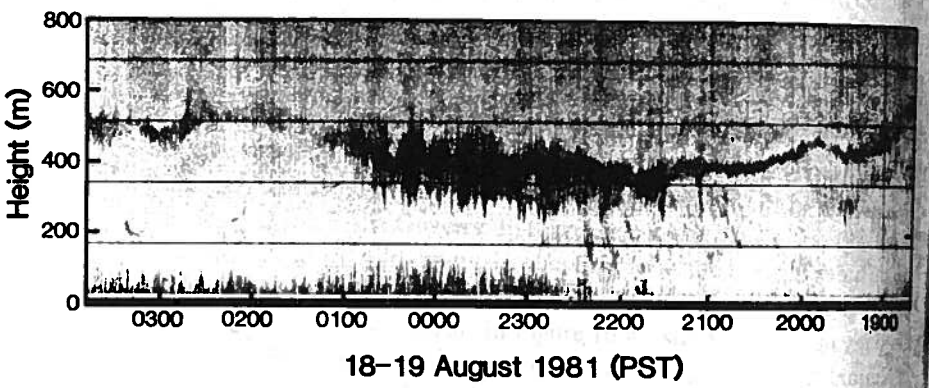

Fig. 8. Example of sodar echo pattern corresponding to low stratus filling the Big Sulphur Creek valley. Variations in the height of the echoes correspond to variations in the height of the stratus layer. The thickness of the layer presumably corresponds to the amount of shear at the top of the cloud and the thickness of the inversion at or above cloud top.

5.6. Dynamical instability

In much of what we have discussed to this point, we have related the origin of acoustic echoes in stably-stratified flows to the effect of a locally-reduced Richardson number following the arguments of Neff and Coulter (1986). An initial reduction of Richardson number below its critical value has also long been related to the formation of quasi

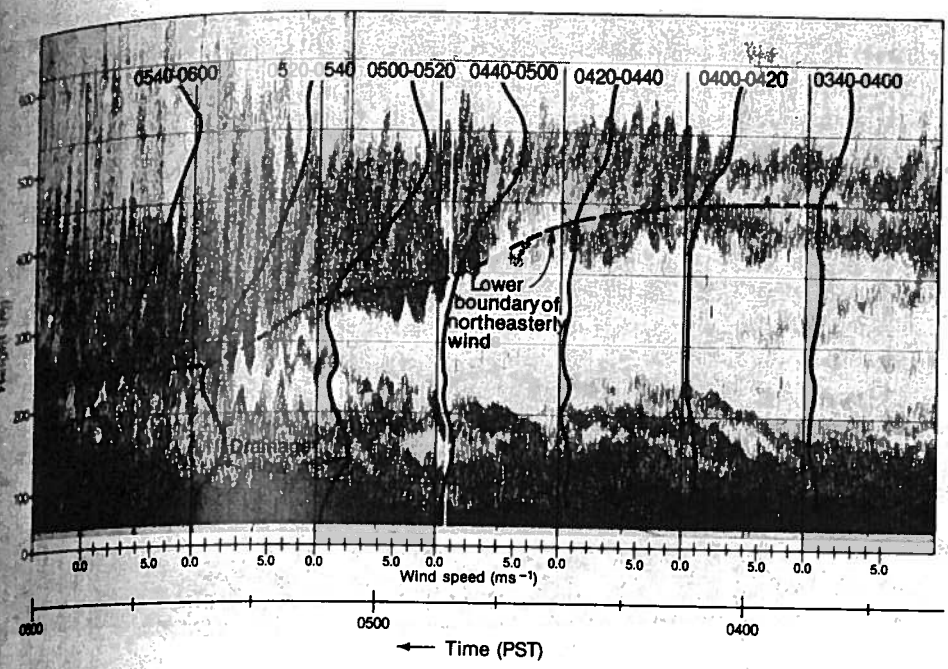

Fig. 9. Sodar echoes showing dynamical instabilities resulting from shear at the top of the nocturnal inversion. In this case, Doppler sodar wind profiles show winds increasing with time and eroding into the stable layer below.

two-dimensional motions, often referred to as Kelvin–Helmholtz instability (e.g., Gossard and Hooke, 1975). As reviewed by Neff and Coulter, such instabilities produce characteristic signatures on sodar facsimile records. In Figure 9, we provide an example of such echoes obtained from the Diamond-D site in the Geysers. In this case, we have superimposed Doppler-derived wind profiles at 20-min intervals showing how the appearance of such echoes often reflects the response to an acceleration of the flow aloft (here from 3 to 8 m s^{-1}) and a consequent increase in the shear. In Figure 10 we show several additional examples of such echoes reflecting their ubiquity in the data from the Diamond-D site, a drainage flow pooling area. Of curiosity in both Figures 9 and 10 is the response of lower-level echo strata to the instabilities above, the same periods of oscillation being present, but with amplitudes that decrease with elevation. This is an example of the 'hydrodynamical filtering' of internal waves, a process that depends on the wavelength of the wave and its frequency relative to the buoyancy frequency of the medium (Gossard and Hooke, 1975).

6. Bistatic Echoes

In general, bistatic echoes, while useful for computation of Doppler shifts from which the winds are deduced, are not usually displayed in facsimile representations. However,

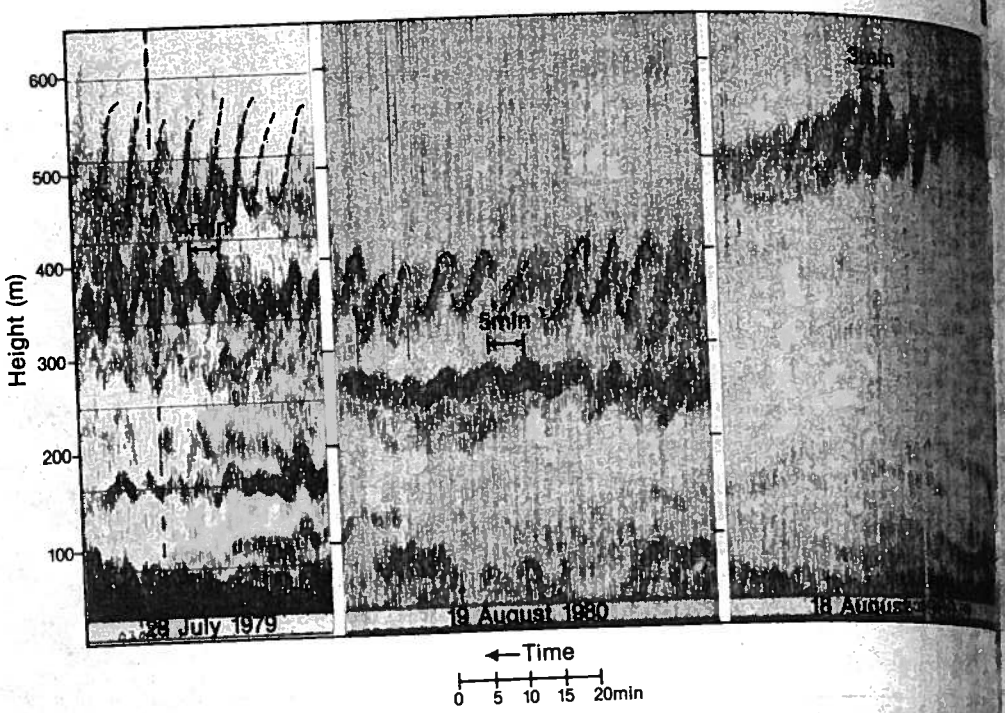

Fig. 10. Similar to Figure 9, but events of smaller scale. Of note in these examples, is the fact that such echoes usually mark the interface between different flows and/or air masses.

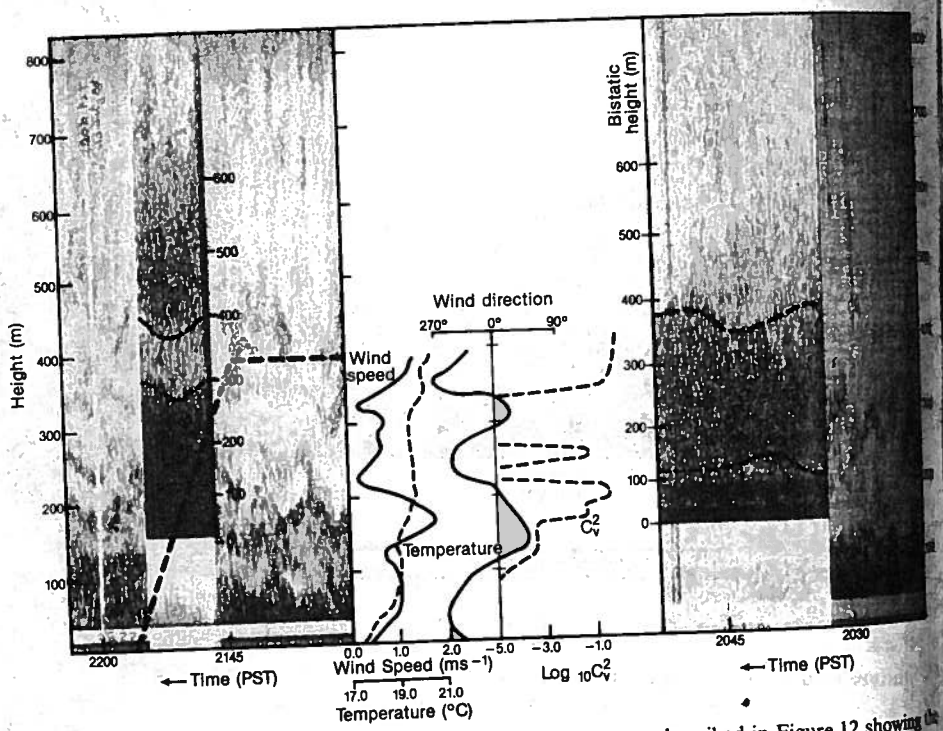

Fig. 11. Example of monostatic and bistatic echoes from the system described in Figure 12 showing the contrast between two types of scattering. The profile of C_v^2 is a model-calculated result using the observed wind and temperature profiles. The difference in vertical scale corresponds to the different travel paths.

from the theory pr
small scales. Their
turbulence in comp
the vertically-poin
surfaces intersecte
depends on the le
the resulting echoe
display and back
arrival of the bistat
scattering occurs i
scales for the two
turbulence fills th
trace at heights be
relative to the mo
of echoes is also
and temperature
period of the nigh
nocturnal drainag

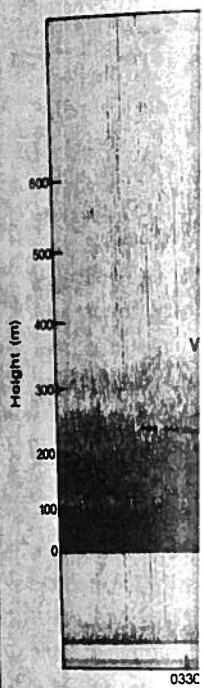

Fig. 12. Extende

from the theory presented earlier, they provide a direct measurement of turbulence at small scales. Their display should, therefore, provide a useful key to the distribution of turbulence in complex terrain flows. At any particular time, the scattering received at the vertically-pointing receiver comes from the volume between the two ellipsoidal surfaces intersected by the vertically pointing beam. The thickness of this ellipsoid depends on the length of the pulse transmitted. Figure 11 shows a typical example of the resulting echoes, where for contrast, we shifted from the monostatic to the bistatic display and back again. Because of the separation of the transmitter and receiver, the arrival of the bistatic pulse is delayed and, in addition, the corresponding height at which scattering occurs is not a linear function of time. This is reflected in the different height scales for the two displays in the figure. In this case, the bistatic echo indicates that turbulence fills the regions between the isolated echo layers shown in the monostatic trace at heights between 100 and 350 m. Above 400 m, the bistatic echoes again increase relative to the monostatic ones, indicating higher levels of turbulence. This distribution of echoes is also reflected in the C_v^2 model-calculated profile obtained using the wind and temperature profile shown in Figure 11. Bistatic traces displayed over a longer period of the night in Figure 12 reveal the variability in space and time of turbulence in nocturnal drainage flows. In particular, this figure shows that turbulence occurs only

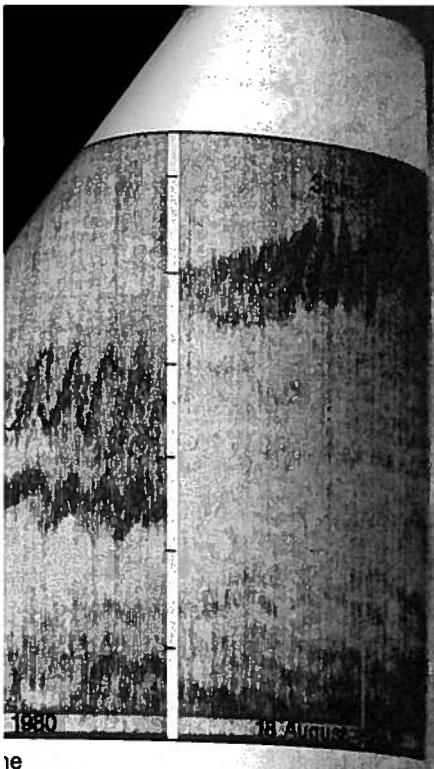

ıe
15 20min

e. Of note in these examples, is the fact that such
n different flows and/or air masses.

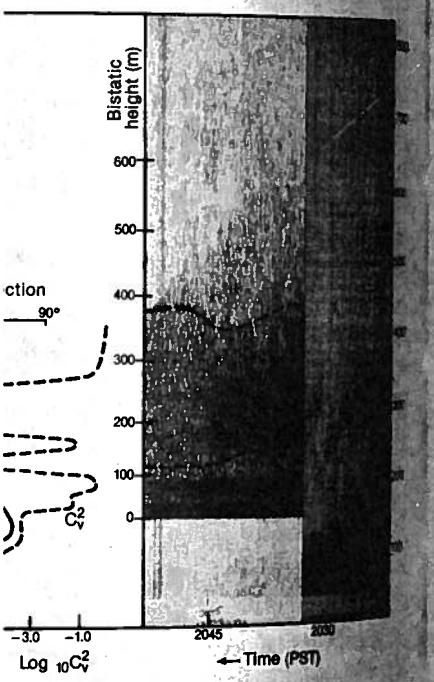

ım the system described in Figure 12 showing the
C_v^2 is a model-calculated result using the observed
al scale corresponds to the different travel paths

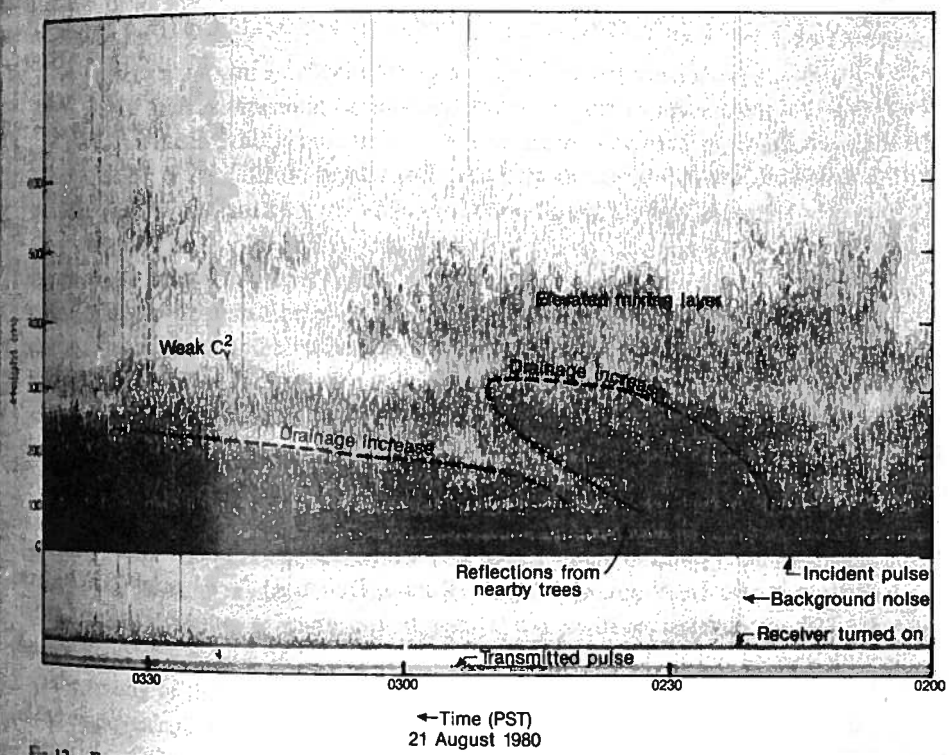

Fig 12. Extended example of bistatic scattering in a drainage flow showing the strong temporal and spatial variability in the distribution of small-scale turbulence.

intermittently above 400 m, and in lamina some 100 to 300 m thick, below this height. Notable also are the regions in which turbulence is very weak. In addition, small-scale turbulence can be seen to increase during surges in the drainage flow.

7. Summary

We have discussed the origin and character of acoustic echoes obtained in complex terrain flows, providing examples interpreted using both tethersonde wind and temperature profiles and Doppler-derived wind profiles. In stably-stratified flows, we found that the scattering cross-sections could be expressed in simple forms with suitable assumptions. This line of reasoning was then developed further using results of a second-order turbulence parameterization that could be used to examine the dependence of scattering on shear and stability in a general fashion and used specifically as a diagnostic tool to analyze wind and temperature profiles measured with a tethered balloon system. We found general agreement between predictions and observations suggesting that further development of such diagnostic tools would be worthwhile.

In the interpretation of monostatic echoes, we found that echo patterns depended sensitively on the distribution of wind and temperature. In simple slope flows and in channeled flows, simple echo patterns were predicted and observed. In complex flows with light and variable winds, echo strata occurred with each reduction of Ri, creating laminated echo patterns.

We also discussed a variety of other echo patterns occurring in complex terrain flows. We found that patterns representing convection with a capping inversion did not reflect the local terrain slope. Stratus and fog, trapped within valleys, revealed themselves with strong echoes at the top of the moist layer. Dynamical instabilities were reflected in distinct echo patterns, usually at the boundaries of different air masses, and in particular when the wind aloft would increase in speed.

Bistatic facsimile recordings, a more unfamiliar product from sodars, showed their ability to depict the distribution of small-scale turbulence in drainage flows. Theoretical analysis using second-order turbulence closure suggested that such bistatic echoes would be dominated by the turbulence portion of the scattering (as oposed to that due to temperature) for all but the largest values of Ri.

Acknowledgements

This research was supported in part by the U.S. Department of Energy, Office of Health and Environmental Research. C. King, H. Ramm, D. Troxel, V. Alvarado, C. Wendt, and R. S. Larsen assisted in various stages of the analysis, engineering, and data collection carried out by WPL.

The essence of Brost
equations lies in (1) th
tions and (2) the para

$$\varepsilon = C_\varepsilon \frac{q^3}{l}$$

where C_ε is a constan
is given by the harmon
scale l_B defined by

$$l_B = C_B \left($$

where $\overline{w^2}$ is the ver
constant. This prescr
displacement availab
stratified temperature
constants in the mode
and neutral surface la
(1979). The resulting
forward algebra, they
number. With this sol
of the variances and
of these solutions. Th

$$C_B \left($$

$$l = z$$

$$C_$$

Because $l = 0$ for (
Richardson number.
$q^2/l^2N_B^2$, $\overline{w^2}/l^2N_B^2$, a
covariance equations
zero at a Richardson
Wyngaard (1979) in t
number.

In the setting of th
fitting model-calculat
functions. In fact, m
covariance equations

Appendix

The essence of Brost and Wyngaard's simplification of the second-moment turbulence equations lies in (1) the dropping of time derivatives, Coriolis terms, and triple correlations and (2) the parameterization of the dissipation rate as

$$\varepsilon = C_\varepsilon \frac{q^3}{l} , \tag{A1}$$

where C_ε is a constant, q^2 is twice the turbulent kinetic energy, and the length scale l is given by the harmonic mean of the distance from the surface, z, and a buoyancy length scale l_B defined by

$$l_B = C_B \left(\frac{\overline{w^2}}{N_B^2} \right)^{1/2} , \tag{A2}$$

where $\overline{w^2}$ is the vertical velocity variance, $N_B^2 = q/T(\partial\theta/\partial z)$, and C_B an empirical constant. This prescription simply relates the dissipation length scale to the vertical displacement available to a fluid parcel moving with vertical velocity w in a stably stratified temperature lapse rate and the height above the surface. The majority of the constants in the model are set through the requirement of matching the observed stable and neutral surface layers as described by Wyngaard (1975) and Brost and Wyngaard (1979). The resulting set of equations is described in Fitzjarrald (1979). With straightforward algebra, they provide a solution for $q^2/l^2N_B^2$ as a function of Richardson number. With this solution, one can then find $\overline{w^2}/l^2N_B^2$. To proceed with a calculation of the variances and covariances requires a prescription for the length scale l in terms of these solutions. This can be obtained from (A2) as

$$l = z \frac{C_B \left(\dfrac{\overline{w^2}}{l^2 N_B^2} \right)^{1/2} - 1}{C_B \left(\dfrac{\overline{w^2}}{l^2 N_B^2} \right)^{1/2}} = z F_l(\mathrm{Ri}) . \tag{A3}$$

Because $l = 0$ for $(\overline{w^2}/l^2N_B^2)^{1/2} = 1/C_B$, the choice of C_B determines the critical Richardson number. This can be seen explicitly in Figure A1 where we have plotted $q^2/l^2N_B^2$, $\overline{w^2}/l^2N_B^2$, and $F_l(\mathrm{Ri})$. From the figure, it is clear that the solution of the covariance equations provides a ratio of buoyant to turbulent time scales that goes to zero at a Richardson number of about 0.43. The choice of $C_B = 1.69$ in Brost and Wyngaard (1979) in turn makes $l = 0$ at an Ri of about 0.23, their critical Richardson number.

In the setting of the model constants, use was made of neutral-layer limits and of fitting model-calculated profiles to stable surface-layer Monin–Obukov similarity functions. In fact, making the approximation $l \approx z$ (i.e., small Ri) allows the set of covariance equations to be reformulated and solved explicitly for the similarity

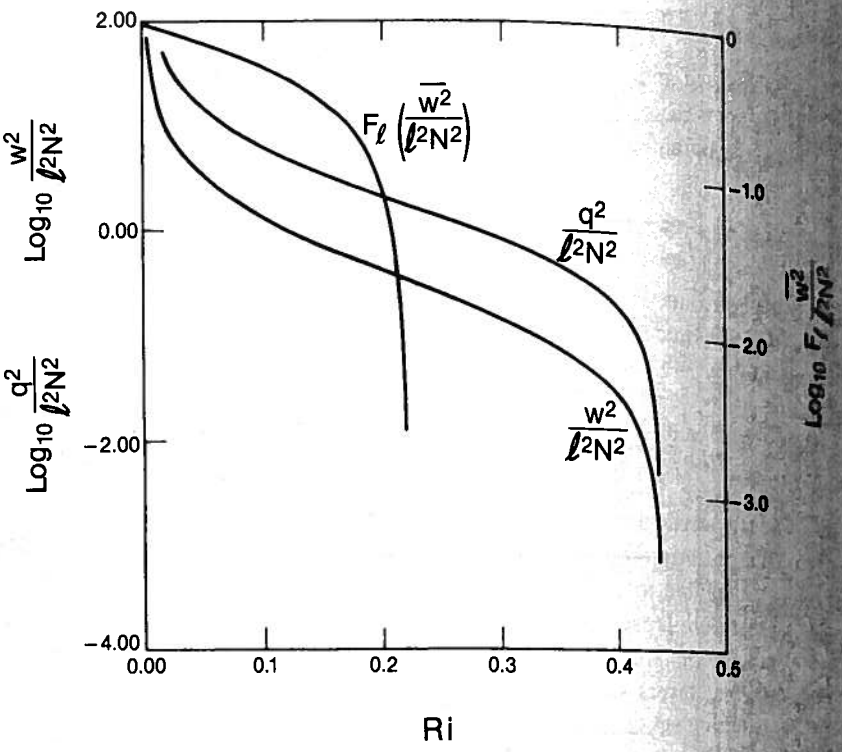

Fig. A1. Behavior of $q^2/l^2N_b^2$ and $\overline{w^2}/l^2N_B^2$ as a function of Ri. The function F_l(Ri) represents the scaling function used in the choice of length-scale parameterization.

functions. This analytical calculation (Neff, 1980) reproduced the results of Brost and Wyngaard (1978), who obtained the similarity function from numerical model calculations, for values of $z/L < 0.2$, where L is the Monin–Obukhov length.

The majority of stable-layer data have been obtained at Ri < 0.25; the inconsistency in the critical Ri described above (Figure A1), therefore, does not normally reveal itself. The question still remains as to how well the model predicts the behavior of turbulence variances and covariances in stably stratified flow for data such as those available from the Kansas experiments. We thus examined the ability of the model to calculate these turbulence quantities, using tabulations of mean gradients, variances, and covariances from the Kansas Data Report (Izumi, 1971). These ratios for temperature flux, stress, and turbulent kinetic energy are presented in Figure A2 as functions of Ri. Least-square fit lines are also shown that reveal the general stability dependence of the results: in these cases the Brost and Wyngaard model underestimates at low Ri, does better with the covariances than variances, and is more credible at Ri greater than 0.1 although the data are more limited. In particular, the temperature flux is least subject to underestimation, the momentum flux somewhat more, and the variance the most. Any non-dimensionalization scheme involving variances and covariances derived from model results should thus reflect an Ri-dependent bias, its magnitude depending on which covariances or

Fig. A2. Ratios of $\overline{uw}$, $\overline{w\theta}$, and

variances are used. (Result
to the model.)

Because the choice of len
fluxes, we also examined th
In Figure A3, we have plo
the model-calculated temp
observed. In these results,
above Ri = 0.1, the choice

A critical feature of the
as $\varepsilon = C_\varepsilon(q^3/l)$. In order to
a subset of the Kansas st
observed turbulent kinetic

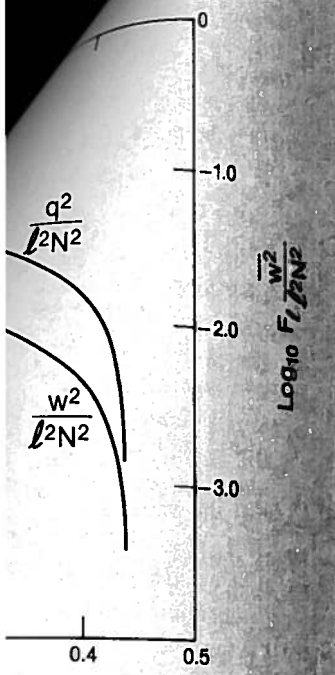

The function F_i(Ri) represents the scaling
e parameterization.

:produced the results of Brost and
ion from numerical model calcula-
n–Obukhov length.
ıed at Ri < 0.25; the inconsistency
ɔre, does not normally reveal itself.
predicts the behavior of turbulence
r data such as those available from
lity of the model to calculate these
dients, variances, and covariances
ratios for temperature flux, stress,
A2 as functions of Ri. Least-square
dependence of the results: in these
tes at low Ri, does better with the
:i greater than 0.1 although the data
is least subject to underestimation,
:e the most. Any non-dimensionali-
derived from model results should
:pending on which covariances or

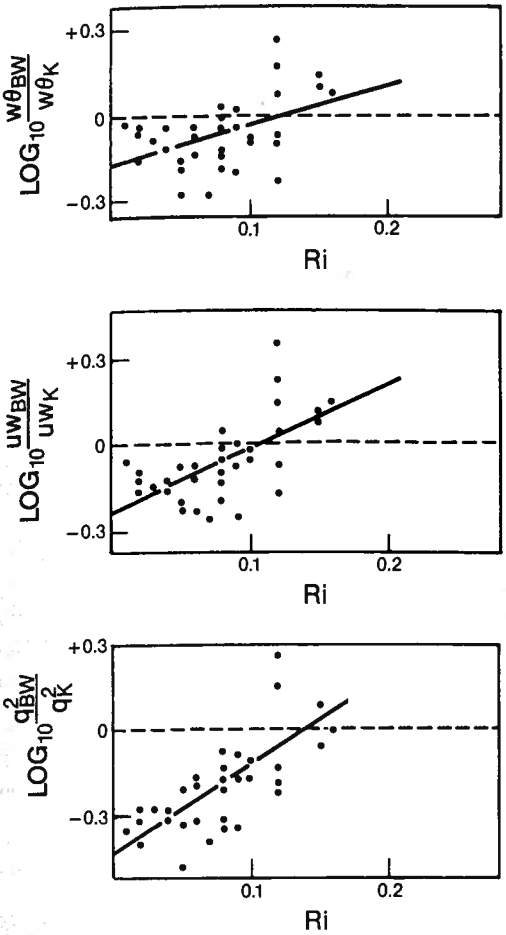

Fig. A2. Ratios of $\overline{uw}$, $\overline{w\theta}$, and q^2 calculated from the model to those observed, as a function of Ri. Least-square fit lines are also shown.

variances are used. (Results from Nieustadt (1984) appear to reflect this bias intrinsic to the model.)

Because the choice of length scale is critical to the determination of the variances and fluxes, we also examined the sensitivity of the results in Figure A2 to the value of C_B. In Figure A3, we have plotted the values of C_B as a function of Ri, required to make the model-calculated temperature flux and turbulent kinetic energy agree with those observed. In these results, C_B has the greatest stability dependence below Ri = 0.1; above Ri = 0.1, the choice $C_B = 1.69$ appears quite appropriate for this limited data set.

A critical feature of the model used is in the parameterization of the dissipation rate as $\varepsilon = C_\varepsilon(q^3/l)$. In order to test this parameterization, we obtained dissipation rates for a subset of the Kansas stable runs (J. C. Kaimal, private communication), used the observed turbulent kinetic energy, and calculated the dissipation length scale from (A1).

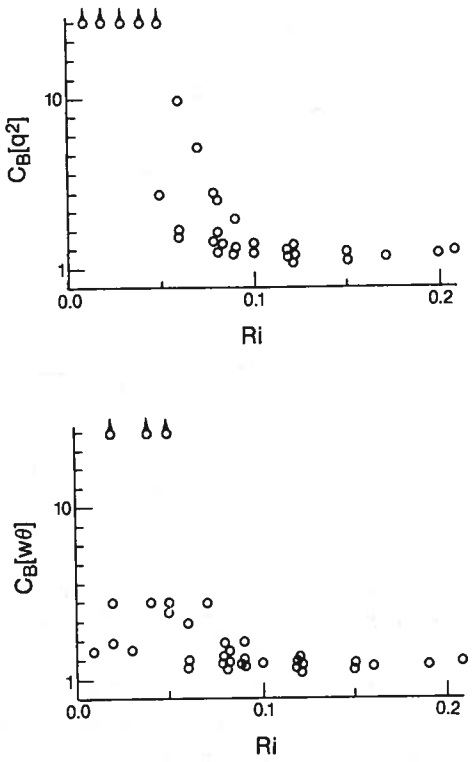

Fig. A3. Values of the length-scale constant C_B required to optimize the fit of model-calculated to observed values of heat flux and total turbulent kinetic energy.

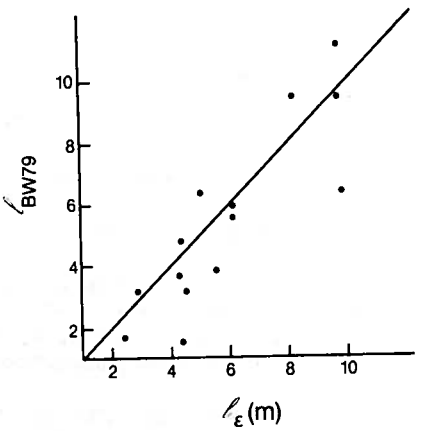

Fig. A4. Scatter plot of model-calculated length scales l_{BW} to those calculated directly from observed dissipation rates and turbulent kinetic energy, l_ε.

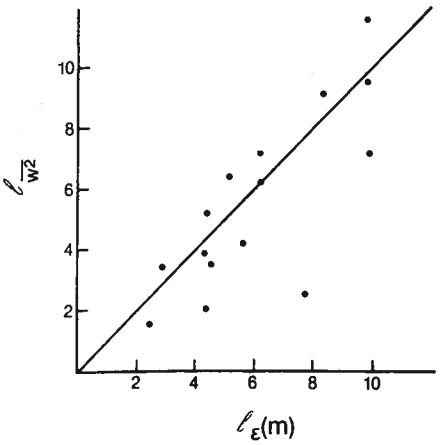

Fig. A5. Length scale calculated from (A2) and observed $\overline{w^2}$, l_w^2, compared with observed dissipation length scale, l_ε.

We then compared this value with that predicted using the mean gradients in the Brost and Wyngaard model (Figure A4) and with that predicted by (A2) using observed values of $\overline{w^2}$ and N_B^2 (Figure A5). The figures show the generally good agreement for these surface-layer results; equivalent data outside the surface layer under more stable conditions (strong static stability, light winds) are limited.

References

Brost, R. A. and Wyngaard, J. C.: 1978, 'A Model Study of the Stably Stratified Planetary Boundary Layer', *J. Atmos. Sci.* **35**, 1427–1440.

Brost, R. A. and Wyngaard, J. C.: 1979, 'Reply', *J. Atmos. Sci.* **36**, 1821–1822.

Burk, S. D.: 1980, 'Refractive Index Structure Parameters: Time-Dependent Calculations Using a Numerical Model', *J. Appl. Meteorol.* **19**, 562–576.

Fitzjarrald, D. E., 1979: 'On Using a Simplified Turbulence Model to Calculate Eddy Difusivities', *J. Atmos. Sci.* **36**, 1817–1820.

Gossard, E. E. and Hooke, W. H.: 1975, *Waves in the Atmosphere*, Elsevier, Amsterdam, The Netherlands, 456 pp.

Horst, T. W. and Doran, J. C.: 1986, 'Nocturnal Drainage Flows on Simple Slopes', *Boundary-Layer Meteorol.* **34**, 263–286.

Izumi, Y. (ed.): 1971, *Kansas 1968 Field Program Data Report*, Air Force Cambridge Research Laboratories, Environmental Research Papers, No. 379 (AFCRL-72–0041), Available Nat. Tech. Inform. Service.

Kaimal, J. C., Abshire, N. L., Chadwick, R. B., Decker, M. T., Hooke, W. H., Kropfli, R. A., Neff, W. D., Pasqualucci, F., and Hildebrand, P. H.: 1982, 'Estimating the depth of the Convective Boundary Layer', *J. Appl. Meteorol.* **21**, 1123–1129.

Manins, P. C. and Sawford, B. L.: 1979, 'A Model of Katabatic Winds', *J. Atmos. Sci.* **36**, 619–630.

Neff, W. D.: 1980, 'An Observational and Numerical Study of the Atmospheric Boundary Layer Overlying the East Antarctic Ice Sheet', Ph.D. Dissertation, University of Colorado, Boulder, 272 pp.

Neff, W. D. and Coulter, R. L.: 1986, 'Acoustic Remote Sensing' in D. H. Lenshow (ed.), *Probing the Atmospheric Boundary Layer*, Amer. Meteorol. Soc. Boston, Mass., pp. 201–236.

Neff, W. D. and King, C. W.: 1987, 'Observations of Complex-Terrain Flows Using Acoustic Sounders: Experiments, Topography, and Winds', *Boundary-Layer Meteorol.* **40**, 363.

Nieuwstadt, F. T. M.: 1984, 'The Turbulence Structure of the Stable, Nocturnal Boundary Layer', *J. Atmos. Sci.* **41**(14), 2202–2216.

Wyngaard, J. C.: 1975, 'Modeling the Planetary Boundary Layer: Extension to the Stable Case', *Boundary-Layer Meteorol.* **9**, 441–460.